Research article

Optical characterization and defect-induced behavior in ZnAl$_{1.999}$Ho$_{0.001}$O$_4$ spinel: Unraveling novel insights into structure, morphology, and spectroscopic features

I. Elhamdi [a,*], H. Souissi [a], O. Taktak [a], S. Kammoun [a], E. Dhahri [a], J. Pina [b], B.F.O. Costa [c], E. López-Lago [d]

[a] *Applied Physics Laboratory, Faculty of Sciences, Sfax University, BP 1171, 3000, Sfax, Tunisia*
[b] *University of Coimbra, CQC-IMS, Chemistry Department, 3004-535, Coimbra, Portugal*
[c] *University of Coimbra, CFisUC, Physics Department, 3004-516, Coimbra, Portugal*
[d] *Departamento de Física Aplicada, Facultade de Óptica e Optometría, Campus Vida, Universidade de Santiago de Compostela (USC), 15782 Galicia, Spain*

A B S T R A C T

The ZnAl$_{1.999}$Ho$_{0.001}$O$_4$ phosphor, prepared by the solid-state method, crystallizes in the cubic spinel structure. Morphology and chemical composition homogeneity were determined via Energy Dispersive X-ray and SEM analysis. The (E$_g$) optical band gap was evaluated from the UV/vis absorption spectrum, confirming direct transition behavior according to Tauc's law. The Urbach energy (Eu) in the ZnAl$_{1.999}$Ho$_{0.001}$O$_4$ spinel was higher than that in the ZnAl$_2$O$_4$ spinel, indicating increased disorder and a higher concentration of defects due to Ho^{3+} ions. The penetration depth ($\delta(\lambda)$), optical extinction ($k(\lambda)$), and refractive index ($n(\lambda)$) were assessed across wavelengths (λ). The room temperature absorption spectrum revealed several peaks corresponding to the 4f-4f transitions of Ho^{3+} ions.

1. Introduction

Spinel is an important material family with remarkable physical properties [1–11]. Its composition obeys a general formula given by AB$_2$X$_4$, A is a metal cation (Zn^{2+}, Mg^{2+}, ….) located at tetragonal site T$_d$, B is a cation (Al^{3+}, Ga^{3+}, …) occupying an octahedral site O$_h$ and X = O, S, …, Optoelectronic devices like photovoltaic solar cells [12], light-emitting diodes [13], and others can benefit from the employment of these materials. Spinels are also thought to be extremely adaptable luminescent matrices with a B-site that can accept various luminescent centers, such as lanthanide (Ln) ions and/or transition metal (TM) ions, resulting in a variety of compounds with appealing luminescent properties [5,6,11]. Recently, using solid-state and sol-gel techniques, we synthesized a novel spinel persistent phosphor of ZnAl$_{0.095}$Cr$_{0.05}$O$_4$ [5,6,11]. Studies have been focused on its structural, electrical, vibrational, and optical characteristics [5,6,11]: the Raman and infrared spectra at ambient temperature have been analyzed; the gap E$_g$ has been established from absorption UV/vis and reflectance Spectra, and Tauc's law has validated the direct transition. The Urbach energy E$_u$ is found to be 0.63 eV for ZnAl$_{1.95}$Cr$_{0.05}$O$_4$ indicating a disorder condition in this spinel. In the O$_h$ site symmetry, the crystal field study was used to identify the electronic structure of Cr^{3+} from the optical spectra [5,6,11]. The Ho^{3+} ion is part of the Lanthanide family with a 4f^{10}

---

* Corresponding author.
E-mail address: imen.elhamdi.etud@fss.usf.tn (I. Elhamdi).

electronic configuration. When it is part of the spinel constitution, a potential up-conversion material emerges due to its large anti-Stokes shift, longer lifetime, high photostability, sharp tunable emissions and ladder-like 4f energy levels [14]. The incorporation of Holmium (Ho^{3+}) into the spinel system was found to introduce defects that significantly influence its optical properties. This study explores the intricate relationship between the presence of Ho^{3+} ions and the induced defects, shedding light on their pivotal role in modulating the optical features of the material. From the comprehensive analysis, including absorption spectra and other optical measurements, we aim to elucidate the specific mechanisms by which the introduced defects impact the optical behavior of the spinel system [15–17]. The spinel $ZnAl_{1.999}Ho_{0.001}O_4$ is an important compound in advanced photonic applications due to the presence of the Ho^{3+} ion, which is an activate center that emits in the shortwave infrared region ($\lambda \sim 1.20$ μm). The main $^5I_7 \rightarrow {}^5I_8$ emission band characterizes the PL spectra of Ho^{3+}.

In this work, $ZnAl_{1.999}Ho_{0.001}O_4$ spinel were prepared by solid-state reaction and characterized by structural and optical techniques to take a decisive step in decoding the complexities inherent in oxide systems. Beyond its contribution to the fundamental understanding of these materials, our study has the potential to influence the development of advanced materials, presenting opportunities for tailoring properties that can be exploited in various applications. This study represents an important undertaking, laying the foundation for advances in the scientific understanding and practical use of oxide materials [18–20].

2. Experimental details

The $ZnAl_{1.999}Ho_{0.001}O_4$ sample was synthesized via solid-state reaction using appropriate mixtures of $ZnCO_3$ (98%), Ho_2O_3(99%), and Al_2O_3 (99%). After annealing at 700 °C, the powders were crushed with an Agate Mortar and Pestle and gradually heated to the sintering temperature at 1200 °C, with a soaking time of 24h. Finally, the powders were compressed into pellets with an 8 mm diameter and annealed at 1200 °C for 24h.

The crystal structures were characterized using an X-ray Diffractometer (X-Ray Siemens D5000) equipped with a CuKα radiation source ($\lambda = 1.5406$ Å). Data collection was performed in the 2θ range of 20°–100° with a step size of 0.02°. A Horiba LabRam HR Evolution micro-Raman confocal system was used to obtain the Raman spectra within the 20-1000 cm^{-1} range, with excitation at 532 nm. The acquisition parameters included an acquisition time of 10 s, 50 accumulations, and a laser power of approximately 17 mW at the sample. Wavenumber calibration was performed using the characteristic Si wafer band at 520.5 cm^{-1}. The morphology of the powder and chemical composition were examined using a TESCAN VEGA3 SBH scanning electron microscope (SEM) to assess compound homogeneity. Solid-state absorption spectra were acquired by measuring the reflectance using an AvaSpec-ULS-TEC Avantes Senseline Fiber Optic Spectrometer System coupled to a Mikropack DH-2000-BAL UV–Vis–NIR light source. A 45-degree angle probe tip fiber optic bundle (FCR-UV200/600-2-IND 1211040) was utilized for reflection measurements in powders and thick fluids. The 45-degree angle of the probe tip prevented direct back reflection from the window. Before determining the spectra of the solid samples, background correction was conducted by acquiring the baseline with 100% and 0% reflectance, using a Polytetrafluoroethylene (PTFE) reference sample and blocking the beam, respectively. A Thermo Scientific Nicolet 6700 device operating in the 400–4000 cm^{-1} range was used to record the FTIR spectra. Room temperature EPR spectra of powder samples were obtained using a MiniScope MS 400 X-band EPR spectrometer (Magenttech Germany), equipped with a Suprasil Nitrogen Dewar (SP Wilmad-LabGlass, USA). The powder samples were placed in a 10 μL glass capillary (Duran Ringcaps, Hirschmann, Germany) for analysis. Structural Analysis (VESTA) software (Version 3 Copyright (C) 2006–2022, Koichi Momma and Fujio Izumi), Visualization Electronic and ImageJ software were employed for data analysis and visualization.

3. Results and discussion

3.1. X-ray diffraction study

The X-ray Diffraction patterns of the $ZnAl_{1.999}Ho_{0.001}O_4$ sample is shown in Fig. 1. Using the standard JCPDS data file [JCPDS. 82–1043], it is evident that the diffraction peaks are well indexed to (220); (311); (400); (331); (422); (333); (511); (440); (620) and
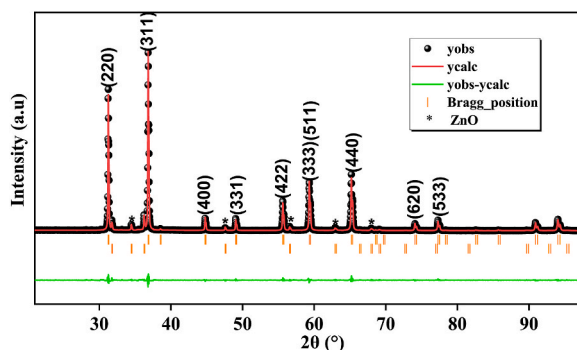

Fig. 1. Rietveld refinement for the $ZnAl_{1.999}Ho_{0.001}O_4$ spinel.

(533) reticular crystal planes of cubic spinel structure phase Fd $\overline{3}$ m space group with lattice parameters a = b = c = 8.0884 Å. Using the Rietveld method, the X-ray diffractogram was refined and confirmed the presence of two phases for the spinel compound: a principal phase $ZnAl_{1.999}Ho_{0.001}O_4$ and an impurity phase with small amounts of ZnO as previously reported [5,21,22]. Table 1 illustrates the refined crystallographic parameters. The χ^2 refinement quality factors indicate the effective goodness of fit between the calculated and observed profiles. The structure of the $ZnAl_{1.999}Ho_{0.001}O_4$ compound is given in Fig. 2. As shown in this figure, the Zn cation resides in tetrahedral coordination (T_d sites), while the Al cation resides in octahedral coordination (O_h sites). The trivalent cation Ho^{3+}, and generally the lanthanides Ln^{3+}, substitute in the octahedral site of the Al^{3+} ions (Fig. 2) [23,24].

The calculated density was determined by the formula [26]:

$$\rho_{th} = \frac{ZM}{VN_A} \tag{1}$$

where $N_A = 6.02 \times 10^{23}$ mol^{-1} stands for the Avogadro number, Z = 8 represents the number of the unit cells for a cubic structure and M is the molar mass of the compound.

While the experimental density was calculated using the following formula [27]:

$$\rho_{exp} = \frac{m}{\pi h r^2} \tag{2}$$

The radius, thickness, and mass of the pellet are represented by r, h, and m, respectively.

The difference between the theoretical and experimental density was evaluated by the following equation to assign the idea of porosity [28]:

$$P(\%) = \frac{\rho_{th} - \rho_{exp}}{\rho_{th}} \text{ x100} \tag{3}$$

The X-ray density ρ_{th} and the porosity P (%) are shown in Table 1.

It was found that the density value of $ZnAl_{1.999}Ho_{0.001}O_4$ is equal to 2.321$_9$ g cm^{-3}. When comparing densities, the experimental density is lower than the theoretical density. Indeed, the sample prepared in practice has internal pores. Additionally, adding a small amount of Holmium has virtually no effect.

To calculate the average crystallite size we used the Williamson–Hall relation D_{W-H} [29,30]:

$$\beta \cos(\theta) = \frac{K\lambda}{D_{W-H}} + 4\varepsilon \sin(\theta) \tag{4}$$

where λ (1.5406 Å) is the wavelength, ε is the effective strain, β is the full-width at half maximum (FWHM), θ is the Bragg angle and K is the shape factor.

The value of the crystallite size was determined by the intercept of the linear fit of $\beta\cos(\theta)$ as a function of $4\sin(\theta)$ (Fig. 3). Accordingly, the D_{W-H} values of this compound is illustrated in Table 1.

3.2. SEM and EDX study

By the use of Scanning electron microscopy (SEM), we estimate the microstructure and morphology of $ZnAl_{1.999}Ho_{0.001}O_4$ spinel. As shown in Fig. 4, the grains are agglomerated with irregular shapes. In fact, the large surface area of the particles and their interaction with the weak van der Waals force are the causes of these agglomerations. Using ImageJ software, the average particle size distribution was found centered at 331 nm by the Lorentz fit, as shown in Fig. 4. Additionally, we displayed the energy dispersion spectrum (EDS) of $ZnAl_{1.999}Ho_{0.001}O_4$ in Fig. 5 to confirm their chemical composition. The spectrum affirms the presence of all the constituent chemical elements of Ho^{3+} substituted $ZnAl_2O_4$, such as Zn, Al, Ho and O, which demonstrates the purity of our sample.

Table 1
Results of Rietveld refinements.

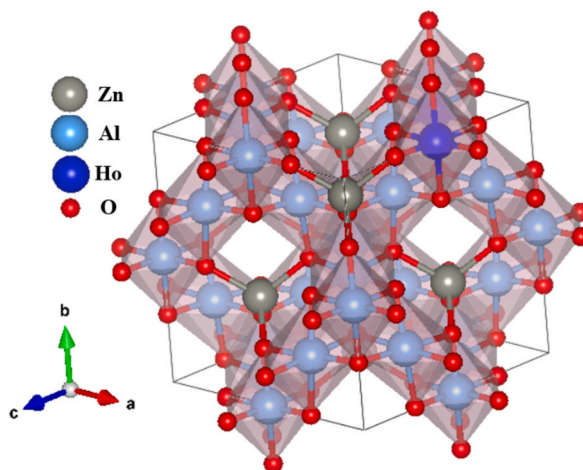| Samples	$ZnAl_{1.999}Ho_{0.001}O_4$
Space Group	Fd $\overline{3}$ m
a(Å)	8.088$_4$
V(Å^3)	529.161$_1$
R$_p$	7.68
R$_{wp}$	8.75
χ^2	3.04
Al–O (Å)	1.919$_1$
Al–O–Al (°)	96.330$_9$
ZnO (%)	4.84
ρ_{th} (g cm^{-3})	4.608$_6$
ρ_{exp} (g cm^{-3})	2.321$_9$
P(%)	49.618$_1$
DW-H (nm)	67

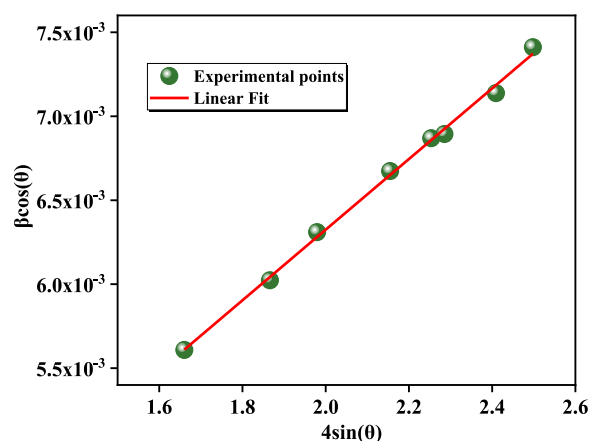Fig. 2. Structural Figure with Vesta software of $ZnAl_{1.999}Ho_{0.001}O_4$ spinel [25].

Fig. 3. The Williamson-Hall plot of $ZnAl_{1.999}Ho_{0.001}O_4$ spinel.

However, the map images presented in Fig. 5 reveal a homogeneous and uniform distribution of the constituent chemical elements of this material. The quantitative analysis of elements presented in the spinel $ZnAl_{1.999}Ho_{0.001}O_4$ is shown in Table 2.

3.3. Raman and FTIR study

Raman spectroscopy is recognized as a crucial analytical tool for phase structure studies, offering greater sensitivity compared to XRD. This heightened sensitivity stems from the fact that Raman energy is less penetrating than X-ray excitation energy [31]. The spinel unit cell contains 56 atoms, but the simplest primitive cell can be made with just 14 atoms. According to group theory, which is presented first by White and DeAngelis [32], spinels possess 42 normal modes divided into 39 optical and 3 acoustic modes at the Brillouin zone center. These modes can be shown in terms of symmetry species given by Equation (5):

$$\Gamma(k = 0) = A_{1g}(R) \oplus E_g(R) \oplus 3T_{2g}(R) \oplus 5T_{1u}(IR) \oplus T_{1g} \oplus 2A_{2u} \oplus 2E_u \oplus 2T_{2u} \tag{5}$$

where R and IR correspond to Raman and infrared-active, respectively. Five modes are Raman active ($A_{1g} + E_g + 3T_{2g}$) and one mode is Infrared active T_{1u} (IR) [33,34]. The A_{1g}, E_g and $3T_{2g}$ modes are, respectively, one, doubly and triply degenerate. These five modes are observed in the case of spinel structures. The Raman spectra of the cubic direct spinel structure of $ZnAl_{1.999}Ho_{0.001}O_4$, belonging to the Fd $\overline{3}$ m space group, agree well with the literature [32,34] and have been shown in Fig. 6. Table 3 illustrate the observed frequencies of these phonons.

High-intensity prominent peaks at 658 cm^{-1} and 416 cm^{-1} correspond to T_{2g} mode (movement of oxygen atoms within AlO_6 octahedra) and E_g (asymmetric bending movement of oxygen atoms in ZnO_4 tetrahedra), respectively. Other modes are observed with relatively low intensities bands at 517 cm^{-1} and 195 cm^{-1} are assigned to T_{2g} mode. However, as the cationic species change, the peak positions and intensities change [22]. The highest frequency movements (>250 cm^{-1}) are mainly due to O and Al ions and the lower
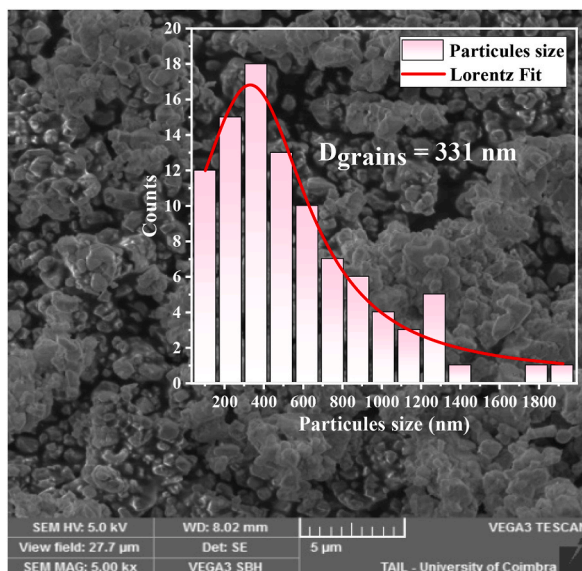
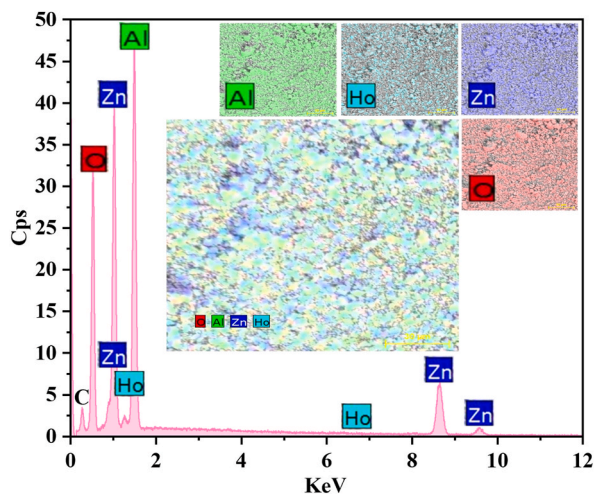**Fig. 4.** SEM image and the average particle size histograms of $ZnAl_{1.999}Ho_{0.001}O_4$ spinel.

Fig. 5. EDS spectrum of $ZnAl_{1.999}Ho_{0.001}O_4$ spinel.

Table 2
EDX data of $ZnAl_{1.999}Ho_{0.001}O_4$ spinel.

Element/Symbol	Series	Atomic (%)	Error (%)
Aluminum/Al	K-series	61.83	6.31
Holmium/Ho	K-series	1.23	0.26
Zinc/Zn	K-series	36.94	1.09

ones are due to Zn, with a dominant contribution of O [35]. It is evident from Fig. 6 that the peaks assigned to T_{2g} mode were asymmetric, indicating the presence of a disorder in spinel.

The FTIR spectra for the spinel in the 400–4000 cm^{-1} spectral range are seen in Fig. 7. The sample has extreme bands peaking at 663, 556 and 478 cm^{-1} which are assigned to Al–O/Ho–O and Zn–O stretching vibrations modes of T_{1u} mode symmetry.

3.4. Determination of the band-gap energy

Fig. 8 portrays the UV–Visible absorption coefficient $\alpha(\lambda)$ of the $ZnAl_{1.999}Ho_{0.001}O_4$ spinel, recorded at ambient temperature in the

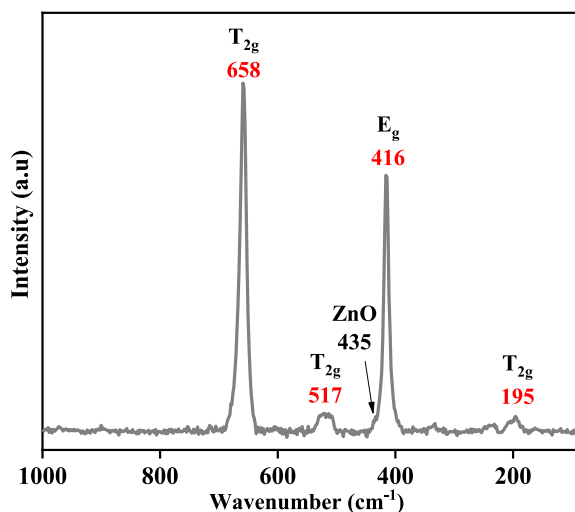**Fig. 6.** Raman spectrum of the $ZnAl_{1.999}Ho_{0.001}O_4$ sample collected using a green laser line at 532 nm.

Table 3
Observed IR and Raman bands (in cm^{-1}) for $ZnAl_{1.999}Ho_{0.001}O_4$ spinel.

	Raman modes	Infrared modes
T_{1u}	–	663
T_{2g}	658	–
T_{1u}	–	556
T_{2g}	517	–
T_{1u}	–	478
E_g	416	–
T_{2g}	195	–

range 300–800 nm. The absorption peaks in the mid-infrared region 400–800 nm may be associated with crystal field transitions of Holmium. Understanding the optical absorption behavior of holmium in this range is relevant for applications in areas such as solid-state physics, materials science, and potentially in the development of optical devices. Fig. 8 presents the absorbance spectrum (in arbitrary units) as a function of wavelength. The Beer-Lambert Law is expressed as [36]:

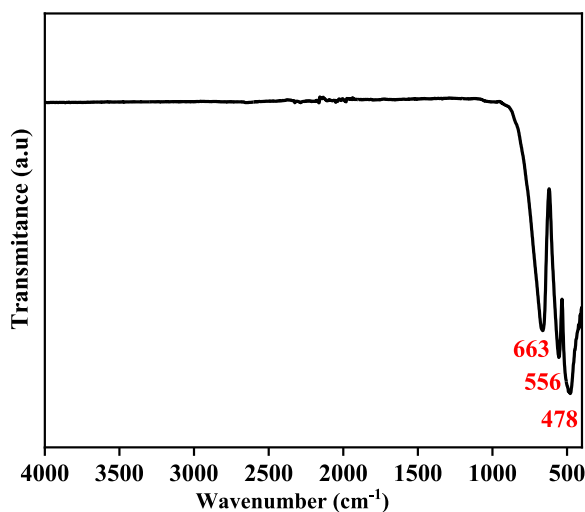$$A = log\left(\frac{I}{I_0}\right) = 0.4343\, \alpha d \qquad (6)$$

Fig. 7. FTIR spectrum of $ZnAl_{1.999}Ho_{0.001}O_4$ spinel.

Where A is the absorbance, I_0 is the intensity of the incident light, I is the intensity of the transmitted light, α is the absorption coefficient and d is the sample thickness. To obtain the band gap energy of the $ZnAl_{1.999}Ho_{0.001}O_4$ spinel, first the absorption coefficient (α) was estimated according to the formula:

$$\alpha(h\nu) = \frac{2.303\,A}{d} \tag{7}$$

where h is the Planck constant and ν is the photon's frequency.

In general, the well-known quadratic equation [37] named as Tauc law relates the absorption coefficient (α) to photon energy (hν) by the following formula:

$$\alpha = \frac{A}{h\nu}(h\nu - E_g)^m \tag{8}$$

$$(\alpha h\nu)^{1/m} = A\,(h\nu - E_g) \tag{9}$$

where A is a constant named the band tailing parameter, E_g is the band gap and m is the power factor described the transition mode, it varies depending on whether the material is amorphous or crystalline. For crystalline compounds, direct transitions can be confirmed by the Tauc's relation [37,38]. For the $ZnAl_{1.999}Ho_{0.001}O_4$ spinel, put m = ½, hence:

$$(\alpha h\nu)^2 = A\,(h\nu - E_g) \tag{10}$$

Hence, plotting $(\alpha h\nu)^2$ against the photon energy (hν) yields a straight line within a specific range. Extrapolating this line to intercept the (hν)-axis provides the value of the direct optical energy gap, Eg Ref. [39]. Fig. 9 illustrates the behavior of the direct optical energy gap, Eg, for our material. The optical band gap is estimated to be 3.44 eV.

For confirming the nature of the optical band transition, we have reorganized equation (9) as following:

$$Ln(\alpha h\nu) = LnA + m\,Ln(h\nu - E_g) \tag{11}$$

Fig. 10 represents the evolution of Ln(α hν) against Ln(hν- 3.44). A straight line is obtained whose slope gives the factor (m). For E_g = 3.44 eV, m is close to 1/2 assuring the direct transitions behavior of the studied sample is illustrated in Fig. 10. The wide band gap of this spinel is an improve of the semiconductor character and its application in optoelectronic devices [40]. As reported in the article by I. Elhamdi et al. [5], we observed an increase in the gap energy when estimating it for Ho-substituted spinel. This variation implies that the gap energy decreases as particle size increases.

3.5. Determination of Urbach energy E_u

The Urbach energy E_u, which rises from phonon dynamics and statistical structural disordering, is an important parameter that characterizes disordered and amorphous materials. This parameter is determined from the Urbach model [41] and is assigned to the width of the tail describing the localized states between conduction and valence bands. A high Urbach energy value indicates significant disorder, often resulting from the introduction of a large concentration of foreign atoms into the structure. This typically leads to a reduction in the effective optical gap. The Urbach energy (Eu) value can be calculated using the following relations, where B is a

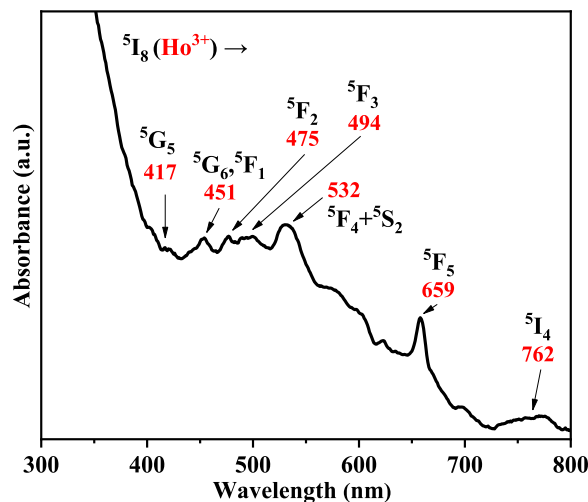**Fig. 8.** Absorbance spectrum at room temperature. Intra-4f absorption pics from the $^5I_8$ ground state to the excited states of Ho^{3+} are showed.
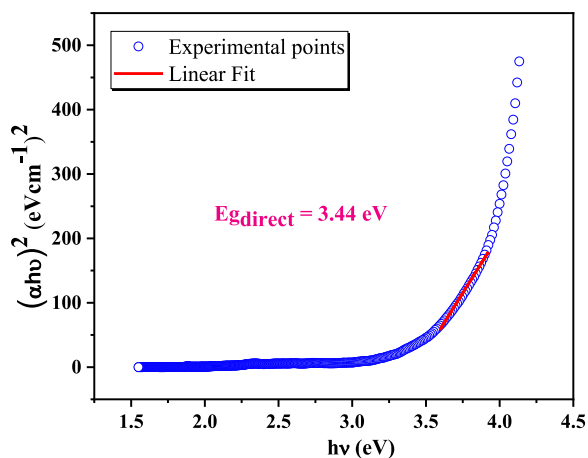
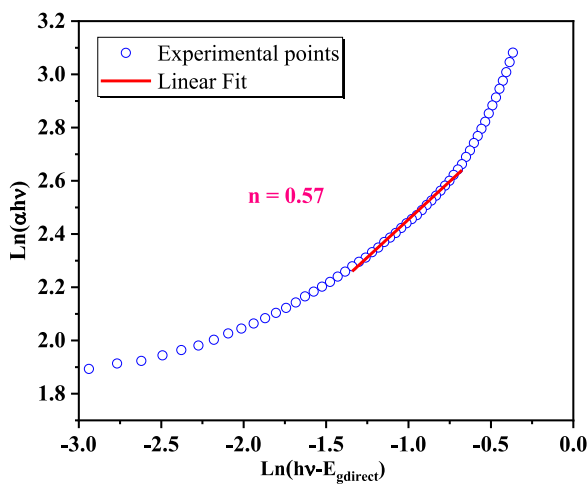**Fig. 9.** Evolution of $(\alpha h\nu)^2$ with the energy hν relative to $ZnAl_{1.999}Ho_{0.001}O_4$ spinel.

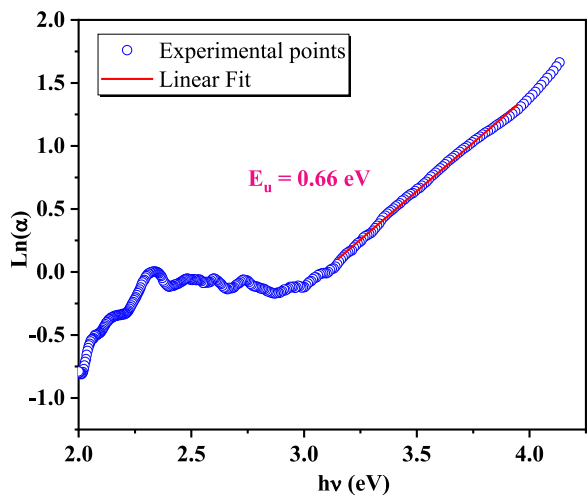**Fig. 10.** Evolution of Ln($\alpha h\nu$) against Ln(hν - 3.44) for $ZnAl_{1.999}Ho_{0.001}O_4$ spinel.

Fig. 11. Variation of Ln(α) with Photon Energy (hν) for Determination of Urbach Energy (Eu) in $ZnAl_{1.999}Ho_{0.001}O_4$ spinel.

constant:

$$\alpha(h\nu) = Bexp\left(\frac{h\nu - Eg}{E_u}\right) \quad (12)$$

$$Ln\ (\alpha) = Ln\ (B) + \frac{h\nu - Eg}{Eu} \quad (13)$$

In Fig. 11, the slope of the curve $Ln(\alpha)$ versus energy $h\nu$ yields a value of Eu = 660 meV, representing 19.18% of the energy bandgap. This indicates significant disorder in the $ZnAl_{1.999}Ho_{0.001}O_4$ spinel.

Comparing the Urbach energy of $ZnAl_2O_4$ at 48 meV, as reported in the article by I. Elhamdi et al. [5], we observe a rise in the Urbach energy when estimating it for $ZnAl_{1.999}Ho_{0.001}O_4$ spinel. This observation implies that there has been an augmentation in disorder and defects concentration within the Holmium-substituted material. It also signifies a higher density of localized states in this material, as indicated in Ref. [5].

3.6. Penetration depth and optical extinction

It is widely acknowledged that when light traverses a sample, some of the incident photon flux is attenuated as certain radiation is absorbed by the material. Therefore, we employed the concept of penetration depth (or skin depth, δ) to illustrate how deep light or incident radiation can penetrate our investigated compound.

We calculated the penetration depth (δ) based on the absorption data using the following equation:

$$\delta(\lambda) = \frac{1}{\alpha(\lambda)} \quad (14)$$

Fig. 12 presents the relationship between incident wavelength and penetration depth for the $ZnAl_{1.999}Ho_{0.001}O_4$ spinel. As illustrated, there is a significant reduction in penetration depth as photon energy increases. This phenomenon could be explained by the decrease in incident photon energy near the material's surface, potentially influencing neighboring Ho^{3+} ions.

In summary, the reduction in penetration depth with increasing photon energy observed in Fig. 12 for the $ZnAl_{1.999}Ho_{0.001}O_4$ spinel is likely due to the material's absorption and optical properties, dependent on its electronic structure. This phenomenon is crucial for understanding how different wavelengths of light interact with the material and can have implications for various applications, such as optical devices and sensors.

The extinction coefficient (k) quantifies the absorption and scattering of light within a medium per unit distance. We determined the extinction coefficient using the following formula:

$$k = \frac{\alpha\lambda}{4\pi} \quad (15)$$

where α is the absorption coefficient.

The spectral distribution of the extinction coefficient is shown in Fig. 13. The extinction coefficient has been found to decrease as wavelength increase. Our findings closely align with those reported by Marquez et al. [42], exhibiting a similar trend to the results presented by El-Sayed and Amin [43].

3.7. Refractive index

Measuring the refractive index (n) is essential when designing components for optical devices [44–46]. The coefficient k, which relates to reflectance and extinction, can be expressed in the following manner:

$$n = \frac{1 + R}{1 - R} + \sqrt{\frac{4R}{(1 - R)^2} - k^2} \quad (16)$$

Fig. 14 depicts the variation of n versus wavelength for the $ZnAl_{1.999}Ho_{0.001}O_4$ sample. As observed, the refractive behavior of our compound exhibits high sensitivity to changes in wavelength. Upon comparison with $ZnAl_2O_4$ [5], a reduction in the refractive index is seen in the doped spinel. This phenomenon may be qualified to the presence of Ho^{3+} ions in the substituted material, which modifies the density of localized states. This information is important in understanding the impact of doping on the electronic behavior of materials and is valuable in various applications such as semiconductor, optoelectronics devices and energy storage.

To characterize the n index of our sample, we employ the Cauchy dispersion relationship, which is expressed as follows [47,48]:

$$n(\lambda) = n_0 + \frac{A}{\lambda^2} + \frac{B}{\lambda^4} \quad (17)$$

where (n_0, A, B) correspond to the Cauchy's constants and λ is the wavelength of the incident photons. The obtained values for n_0, A and B are respectively 2.39, 0.339 $(\mu m)^2$ and 0.035 $(\mu m)^4$ (Fig. 15). The obtained results closely align with those reported in the literature with TPA-CoBr$_4$ [49] and DMA-CoCl$_4$ [50].
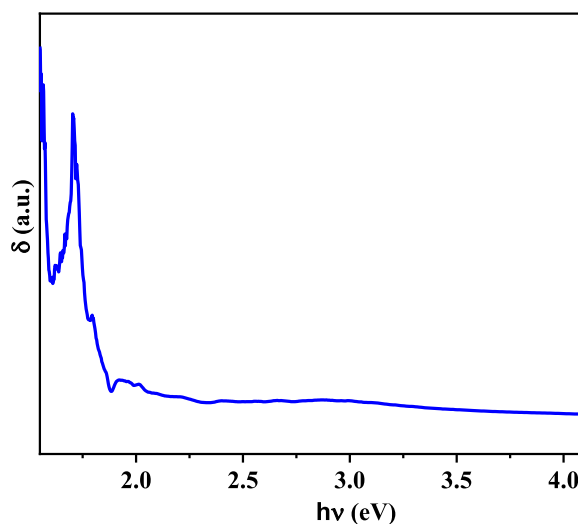
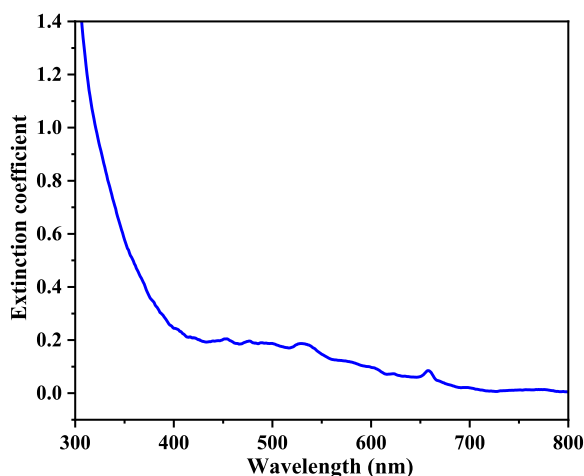**Fig. 12.** Variation of δ versus energy for the $ZnAl_{1.999}Ho_{0.001}O_4$ spinel.

Fig. 13. Evolution of k versus wavelength for the $ZnAl_{1.999}Ho_{0.001}O_4$ spinel.

3.8. The 4f-4f transition of Ho^{3+} ions in $ZnAl_{1.999}Ho_{0.001}O_4$ spinel

The spectrum of Fig. 8 shows several absorption peaks at 417, 451, 475, 494, 532, 659 and 762 nm. these peaks are attributed to the 4f-4f transitions of holmium with $4f^{10}$ electronic configuration [51]. The 3d-3d transitions of the metal ions are highly responsive to variations in the local environment, often resulting in broad absorption and emission bands [52–57]. On the contrary to metal transition ions, the 4f electrons optically active for the lanthanides are screened by the $4s^2 4p^6$ layers. Then these electrons weakly feel the effects of the outside and it is a weak crystal field. The rare earth ions optical spectra are characterized by narrow 4f-4f transitions. Furthermore, the positions of these transitions are almost identical to those of the free ion and don't depend on the host matrix in which they are incorporated. For this reason, the assignment of the 4f-4f transitions of Ho^{3+} is based on the comparison with energy level scheme of Ho^{3+} in $HoCrO_3$ perovskite compound [51]. Also, the weak crystal field effect allows for consistency in the energy transitions, resulting in similar absorption and emission spectra for rare earth elements across various environments. This feature makes rare earth elements valuable for applications in optics, as their predictable and consistent spectroscopic behavior facilitates the design and engineering of materials for specific applications, such as lasers, phosphors, and other optoelectronic devices. Table 4 presents the Ho^{3+} transitions from the ground state $^5I_8$ (Ho^{3+}) to different excited states. The presence of these transitions indicates that the incorporation of Ho^{3+} ions into the normal spinel $ZnAl_{1.999}Ho_{0.001}O_4$ has been successful. From Fig. 8, we remark that the absorption bands $^5I_8(Ho^{3+}) \rightarrow {}^5G_5(Ho^{3+})$ (417 nm), $^5I_8(Ho^{3+}) \rightarrow {}^5G_6(Ho^{3+})\ {}^5F_1(Ho^{3+})$ (451 nm), $^5I_8(Ho^{3+}) \rightarrow {}^5F_2(Ho^{3+})$ (475 nm), $^5I_8(Ho^{3+}) \rightarrow {}^5F_3(Ho^{3+})$ (494 nm), $^5I_8(Ho^{3+}) \rightarrow {}^5F_4(Ho^{3+}) + {}^5S_2(Ho^{3+})$ (532 nm), $^5I_8(Ho^{3+}) \rightarrow {}^5F_5(Ho^{3+})$ (659 nm) and $^5I_8(Ho^{3+}) \rightarrow {}^5I_4(Ho^{3+})$ (762 nm) are relatively intense and sharp.

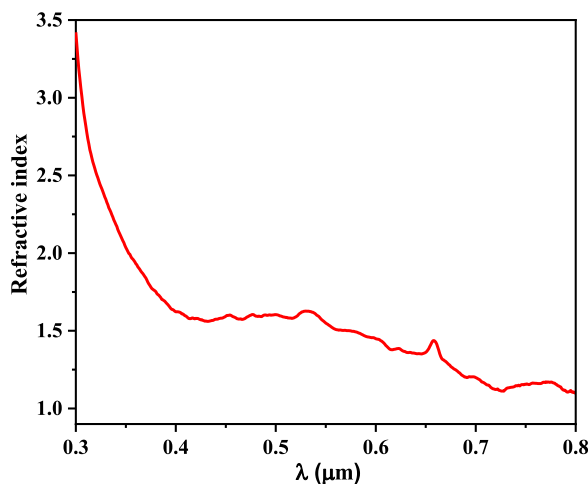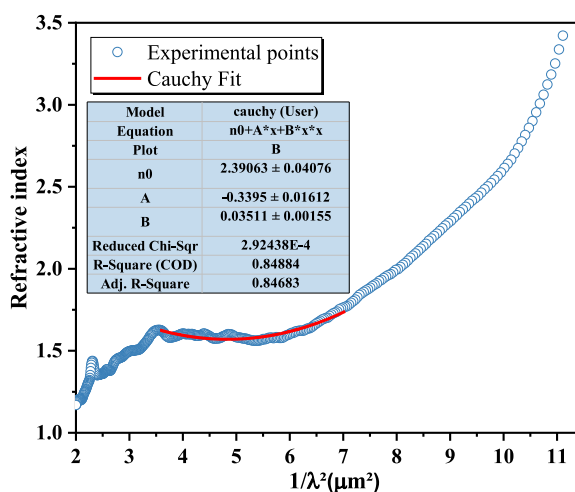**Fig. 14.** Evolution of n as a function of the incident photon wavelength λ for the ZnAl$_{1.999}$Ho$_{0.001}$O$_4$ spinel.

Fig. 15. Plot of the refractive index versus $1/\lambda^2$ for ZnAl$_{1.999}$Ho$_{0.001}$O$_4$ spinel.

3.9. Electronic paramagnetic resonance (EPR)

Electronic paramagnetic resonance (EPR) or electron spin resonance (ESR) spectroscopy is a magnetic resonance technique for detecting the resonance transitions between energy states of unpaired electrons in an applied magnetic field. This technique is particularly useful for studying paramagnetic species and their electronic structure. Fig. 16 shows the EPR spectrum of ZnAl$_{1.999}$Ho$_{0.001}$O$_4$ spinel recorded at room temperature. The rare earth ion Ho^{3+}, with electronic configuration 4f^{10}, is a non-Kramer's ion. This ion is EPR silent in theory. The g-factor is a dimensionless quantity that characterizes the splitting of energy levels in magnetic systems.

Table 4
4f-4f (Ho^{3+}) absorption energy (in nm) for ZnAl$_{1.999}$Ho$_{0.001}$O$_4$ spinel.

Peaks	Transitions
417	$^5I_8(Ho^{3+}) \rightarrow {}^5G_5(Ho^{3+})$
451	$^5I_8(Ho^{3+}) \rightarrow {}^5F_1, {}^5G_6(Ho^{3+})$
475	$^5I_8(Ho^{3+}) \rightarrow {}^5F_2(Ho^{3+})$
494	$^5I_8(Ho^{3+}) \rightarrow {}^5F_3(Ho^{3+})$
532	$^5I_8(Ho^{3+}) \rightarrow {}^5F_4(Ho^{3+}) + {}^5S_2(Ho^{3+})$
659	$^5I_8(Ho^{3+}) \rightarrow {}^5F_5(Ho^{3+})$
762	$^5I_8(Ho^{3+}) \rightarrow {}^5I_4(Ho^{3+})$

The g-factor is defined as the ratio of the magnetic moment to the angular momentum of a particle. For electrons, the g-factor is approximately 2.0023, but it can be influenced by the local environment and the nature of the magnetic interaction. Fig. 17 displays several resonance signals with effective g values measured at g = 4.5, 3.87, and 2.0. Three values are also observed in the EPR spectra of Cr^{3+}-doped Zn_2SnO_4 phosphors (g = 1.99, 3.93 and 4.40) and are assigned to three different traps [58]. These traps are integral to the persistent phosphorescent behavior of Cr^{3+}-doped Zn_2SnO_4 phosphors [56,59]. The V^- centers (a hole trapped at a cation vacancy) and F^+ centers (an electron trapped at an anion vacancy) are the primary centers observed in $ZnAl_2O_4$, identifiable by the resonance peak at g = 2.0 [60]. The EPR spectrum of $ZnAl_2O_4$: Cr^{3+} has been also studied and shows signals at g = 1.960, 2.003 and 2.010 [61]. These signals are assigned to simple ionized oxygen vacancies (g = 1.960), and to superoxide anions (O^{2-}) (g = 2.003 and 2.010). The growing signal strength at about g = 3.84 indicates that there are more emission centers in spinel lattices [62]. The EPR signals observed on Fig. 17 indicates the presence of three type of traps which are instrumental in driving the persistent phosphorescence of $ZnAl_{1.999}Ho_{0.001}O_4$ spinel. As expected, there was no resonance signal at room temperature corresponding to Ho^{3+} ions [63]. The nature of the traps in $ZnAl_{1.999}Ho_{0.001}O_4$ spinel is contingent upon the role played by the holmium ions in the material. If Ho^{3+} acts as a donor, contributing additional electrons to the lattice, it creates donor-type traps. These traps involve specific energy levels within the band gap where electrons become localized. On the other hand, if Ho^{3+} acts as an acceptor, capturing electrons from the lattice, it establishes acceptor-type traps. These traps entail localized states within the band gap, affecting the electronic and optical properties of the materiel.

4. Conclusion

The study of $ZnAl_{1.999}Ho_{0.001}O_4$ significantly contributes to the comprehension of its structural and optical properties. The structural and morphological study establishes a fundamental basis for the crystallographic arrangement and provides insight into the microstructure and uniformity of the synthesized material. Spectroscopic analyses, including room temperature Raman and infrared spectra, provided a comprehensive examination of vibrational modes and structural characteristics. The determination of the band gap (E_g) from the UV/vis absorption spectrum, in accordance with Tauc's law, enhances our understanding of the electronic transitions within the material. The observed higher Urbach energy (Eu) in the $ZnAl_{1.999}Ho_{0.001}O_4$ spinel compared to $ZnAl_2O_4$ signifies increased disorder and a higher concentration of defects, attributed to the presence of Ho^{3+} ions. Additionally, the wavelength-dependent assessment of optical properties and the identification of 4f-4f transitions in the ambient temperature absorption spectrum further contribute to the comprehensive characterization of $ZnAl_{1.999}Ho_{0.001}O_4$. These findings collectively advance our knowledge of the material's behavior, paving the way for potential applications in diverse fields such as optoelectronics and luminescent devices.

Data availability

No data were used for the research described in this article.

CRediT authorship contribution statement

I. Elhamdi: Methodology. **H. Souissi:** Visualization. **O. Taktak:** Writing – original draft. **S. Kammoun:** Supervision. **E. Dhahri:** Supervision. **J. Pina:** Visualization. **B.F.O. Costa:** Visualization, Validation. **E. López-Lago:** Supervision.
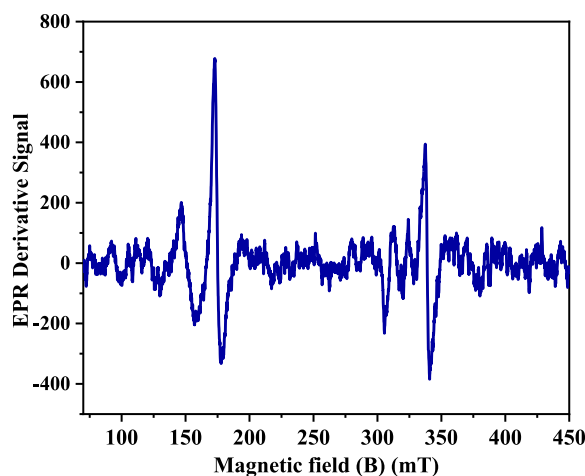

Fig. 16. EPR spectrum of $ZnAl_{1.999}Ho_{0.001}O_4$ spinel at room temperature.

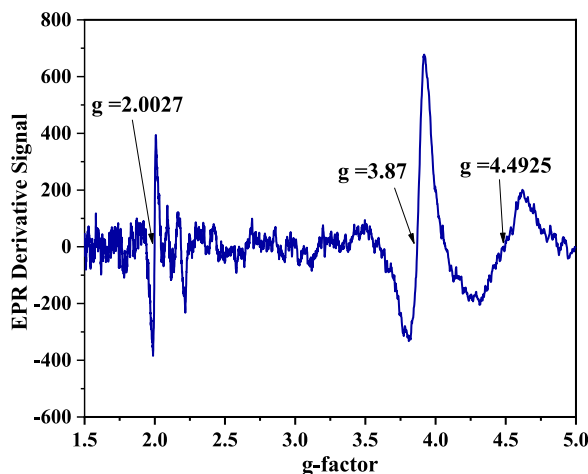**Fig. 17.** The g-factor of $ZnAl_{1.999}Ho_{0.001}O_4$ spinel.

Declaration of competing interest

The authors declare that they have no known competing financial interests or personal relationships that could have appeared to influence the work reported in this paper.

Acknowledgments

References

[1] B. Qiao, Z.L. Tang, Z.T. Zhang, L. Chen, Photoluminescent and electroluminescent characteristics of $ZnGa_2O_4$:Cr^{3+} red phosphor, Acta Phys. Chim. Sin. 22 (10) (2006) 1291–1295.
[2] C.R. Garcia, J. Oliva, L.A. Diaz-Torres, E. Montes, G. Hirata, J. Bernal Alvarado, C. Gomez-Solis, Controlling the white phosphorescence $ZnGa_2O_4$ phosphors by surface defects, Ceram. Int. 45 (2019), 4972–497.
[3] W.A.I. Tabaza, H.C. Swart, R.E. Kroon, Luminescence of Ce doped $MgAl_2O_4$ prepared by the combustion method, Physica B439 (2014) 109–114.
[4] V. Singh, R.P.S. Chakradhar, J.L. Raoc, D.K. Kim, Characterization, EPR and luminescence studies of $ZnAl_2O_4$: Mn phosphors, J. Lumin. 128 (2008) 394–402.
[5] I. Elhamdi, H. Souissi, S. Kammoun, E. Dhahri, A.L.B. Brito, R. Fausto, B.F.O. Costa, Experimental determination and modeling of structural, vibrational and optical properties of the $ZnAl_{2-x}Cr_xO_4$ ($x = 0$ and 0.05) spinels, J. Lumin. 263 (2023) 119968.
[6] I. Elhamdi, F. Mselmi, H. Souissi, S. Kammoun, E. Dhahri, P. Sanguino, B.F.O. Costa, Summerfield scaling model and electrical conductivity study for understanding transport mechanisms of a Cr^{3+} substituted $ZnAl_2O_4$ ceramic, RSC Adv. 13 (2023) 3377–3393.
[7] M.G. Brik, J. Papan, D.J. Jovanović, M.D. Dramićanin, Luminescence of Cr^{3+} ions in $ZnAl_2O_4$ and $MgAl_2O_4$ spinels: correlation between experimental spectroscopic studies and crystal field calculations, Journal ofLuminescence177 (2016) 145–151.
[8] M.T. Tran, D.Q. Trung, N. Tu, D.D. Anha, L.T.H. Thu, N.V. Du, N.V. Quang, N.T. Huyen, N.D.T. Kien, D.X. Viet, N.D. Hung, P.T. Huy, Single-phase far-red-emitting $ZnAl_2O_4$:Cr^{3+} phosphor for application in plant growth LEDs, J. Alloys Compd. 884 (2021) 161077.
[9] S.V. Motloung, F.B. Dejene, H.C. Swart, O.M. Ntwaeaborwa, Effects of Cr^{3+} mol% on the structure and optical properties of the $ZnAl_2O_4$:Cr^{3+} nanocrystals synthesized using sol–gel process, Ceram. Itnl. B 41 (2015) 6776–6783.
[10] S.P. Huang, Z.Q. Wei, X.J. Wu, J.W. Shi, Optical properties of Cr doped $ZnAl_2O_4$ nanoparticles with Spinel structure synthesized by hydrothermal method, Mater. Res. Express 7 (2020) 015025.
[11] I. Elhamdi, F. Mselmi, S. Kammoun, E. Dhahri, A.J. Carvalho, P. Tavares, B.F.O. Costa, A far-red-emitting $ZnAl_{1.95}Cr_{0.05}O_4$ phosphor for plant growth LED applications, Dalton Trans. 52 (2023) 9301–9314.
[12] R.W. Miles, K.M. Hynes, I. Forbes, Photovoltaic solar cells: an overview of state-of-the-art cell development and environmental issues, Prog. Cryst. Growth Char. Mater. 51 (2005) 1–42.
[13] A.A. Bergh, P.J. Dean, Light-emitting diodes, Proc. IEEE 60 (1972) 156–223.
[14] A. Balhara, S.K. Gupta, A.K. Debnath, Kathi Sudarshan, Utilizing energy Transfer in Mn^{2+}/Ho^{3+}/Yb^{3+} Tri-doped $ZnAl_2O_4$ Nanophosphors for tunable luminescence and highly sensitive visual Cryogenic Thermometry, ACS Omega 8 (2023) 30459–30473.
[15] S.E. Shirsath, M. Hussein, N. Assadi, J. Zhang, N. Kumar, A.S. Gaikwad, J. Yang, H.E. Maynard-Casely, Y.Y. Tay, J. Du, H. Wang, Y. Yao, Z. Chen, J. Zhang, S. Zhang, S. Li, D. Wang, Interface-driven Multiferroicity in cubic $BaTiO_3$-$SrTiO_3$ Nanocomposites, ACS Nano 16 (2022) 15413–15424.
[16] Y. Sun, S.E. Shirsath, S. Zhang, D. Wang, A reflection on recent efforts in optimization of cooling capacity of electrocaloric thin films, Apl. Mater. 11 (2023) 090602.
[17] S.E. Shirsath, X. Liu, M.H.N. Assadi, A. Younis, Y. Yasukawa, S.K. Karan, J. Zhang, J. Kim, D. Wang, A. Morisako, Y. Yamauchi, S. Lia, Au quantum dots engineered room temperature crystallization and magnetic anisotropy in $CoFe_2O_4$ thin films, Nanoscale Horiz 4 (2019) 434–444.
[18] J. Wang, P. Wang, W. Chen, F. Wan, Y. Lu, Z. Tang, A. Dong, Z. Lei, Z. Zhang, Highly sensitive multi-pass cavity enhanced Raman spectroscopy with novel polarization filtering for quantitative measurement of SF_6 decomposed components in gas-insulated power equipment, Sensor. Actuator. B Chem. 380 (2023) 133350.

[19] P. Jin, Y. Fu, R. Niu, Q. Zhang, M. Zhang, Z. Li, X. Zhang, Non-destructive detection of the freshness of air-modified mutton based on near-infrared spectroscopy, Foods 12 (2023) 2756.

[20] Y. Qiu, M. Shi, X. Guo, J. Li, J. Wu, Y. Zhou, H. Sun, Y. Hang, X. Li, Y. Li, Sensitivity improvement in the measurement of minor components by spatial confinement in fiber-optic laser-induced breakdown spectroscopy, Spectrochim. Acta B Atom Spectrosc. 209 (2023) 106800.

[21] N.G. Kostova, Al Eliyas, M. Fabián, M. Achimovičová, P. Baláž, Photocatalytic properties of mechanochemically synthesized nanocrystalline $ZnAl_2O_4$ and CdSe, Acta Phys. Pol., A 126 (2014) 967–970.

[22] S.V. Motloung, P. Kumari, L.F. Koao, T.E. Motaung, T.T. Hlatshwayo, M.J. Mochane, Effects of annealing time on the structure and optical properties of $ZnAl_2O_4/ZnO$ prepared via citrate sol-gel process, Mater. Today Commun. 14 (2018), 294-30.

[23] M. Kumar, V. Natarajan, S.V. Godbole, Synthesis, characterization, photoluminescence and thermally stimulated luminescence investigations of orange red-emitting Sm^{3+}-doped $ZnAl_2O_4$ phosphor, Bull. Mater. Sci. 37 (2014) 1205–1214.

[24] V. Singh, G. Sivaramaiah, J.L. Rao, S.J. Dhoble, S.H. Kim, Electron paramagnetic resonance and photoluminescence studies of ultraviolet-emitting $ZnAl_2O_4:Gd^{3+}$ phosphors, J. Electron. Mater. 139 (2015) 1–6.

[25] W.C. Hu, C.H. Kao, F.P. Yang, H.C. Jiau, K.F. Ssu, VESTA: 22nd International Conference on Software Engineering and Knowledge Engineering; SEKE 2010, 2010, pp. 345–348.

[26] D.K. Dasa, J. Sarkarb, Theoretical calculation of atomic and physical properties of some low-dimensional nanomaterials, Mater. Today: Proc. 5 (2018) 27982–27988.

[27] A.V. Humbe, A.C. Nawle, A.B. Shinde, , et al.K.M. Jadhav, Impact of Jahn Teller ion on magnetic and semiconducting behaviour of Ni-Zn spinel ferrite synthesized by nitrate-citrate route, J. Alloys Compd. 691 (2017) 343–354.

[28] S.G. Kakade, R.C. Kambale, C.V. Ramanna, Y.D. Kolekar, Crystal strain, chemical bonding, magnetic and magnetostrictive properties of erbium (Er^{3+}) ion substituted cobalt-rich ferrite ($Co_{1.1}Fe_{1.9-x}Er_xO_4$), RSC Adv. 6 (2016) 33308–33317.

[29] M.Q. Kareem, N.K. Hassan, Evaluation of Williamson–Hall strain and Electrical properties in WO3@NaDCC/ITO nanoparticles thin films prepared by Hydrothermal method, Invention Journal of Research Technology in Engineering & Management (IJRTEM) 3 (2019) 16–26.

[30] I. Elhamdi, H. Souissi, O. Taktak, J. Elghoul, S. Kammoun, E. Dhahri, B.F.O. Costa, Experimental and modeling study of ZnO:Ni nanoparticles for near-infrared light emitting diodes, RSC Adv. 12 (2020) 13074–13086.

[31] J. Feng, T. Liu, Y. Xu, J. Zhao, Y. He, Effects of PVA content on the synthesis of $LaFeO_3$ via sol–gel route, Ceram. Int. 37 (2011) 1203–1207.

[32] W.B. White, B.A.D. Angelis, Interpretation of the vibrational spectra of spinels, Spectrochim. Acta, Part A 23 (1967) 985–995.

[33] A. Kumar, M.A. Dar, P. Sharma, D. Varshney, Structural and Raman scattering study of Ni-doped $CoFe_2O_4$, AIP Conf. Proc. 1591 (2014) 1148.

[34] C.M. Fang, C.K. Loong, G.A. de Wijs, G. de With, Phonon spectrum of $ZnAl_2O_4$ spinel from inelastic neutron scattering and first-principles calculations, Phys. Rev. B 66 (2002) 144301.

[35] V. D'Ippolito, G.B. Andreozzi, F. Bosi, U. Hålenius, L. Mantovani, D. Bersani, R.A. Fregola, Crystallographic and spectroscopic characterization of a natural Zn-rich spinel approaching the endmember gahnite ($ZnAl_2O_4$) composition, Miner. Mag. 77 (2013) 2941–2953.

[36] D.F. Swinehart, The Beer-Lambert Law, vol. 39, 1962, pp. 333–335.

[37] J. Tauc, in: J. Tauc (Ed.), Amorphous and Liquid Semiconductors, Plenum Press, London and New York, 1974.

[38] E.A. Davis, N.F. Mott, Philos. Mag. A 22 (1970) 903.

[39] G.S. Shahane, B.M. More, C.B. Rotti, L.P. Deshmukh, Mater. Chem. Phys. 47 (1997) 263.

[40] S. Kalyanaraman, P.M. Shajinshinu, S.V. Jayalakshmi, Determination of optical constants and polarizability studies on ferroic Tetramethylammonium Tetracholorozincatecrystal, Physica B 482 (2016) 38–42.

[41] M. Ledinsky, T. Schönfeldová, J. Holovský, E. Aydin, Z. Hájková, L. Landová, N. Neyková, A. Fejfar, S. De Wolf, Temperature dependence of the Urbach energy in lead iodide perovskites, J. Phys. Chem. Lett. 10 (2019) 1368–1373.

[42] E. Márquez, A.M. Bernal-Oliva, J.M. González-Leal, R. Prieto-Alcón, A. Ledesma, R. Jiménez-Garay, I. Mártil, Optical-constant calculation of non-uniform thickness thin films of the $Ge_{10}As_{15}Se_{75}$ chalcogenide glassy alloy in the sub-band-gap region (0.1–1.8 eV), Mater. Chem. Phys. 60 (1999) 231–239.

[43] S.M. El-Sayed, G.A.M. Amin, Structure, optical absorption and electrical conductivity of amorphous AsSeGe thin films, Vacuum 62 (2001) 353–360.

[44] A.S. Hassanien, A.A. Akl, Influence of composition on optical and dispersion parameters of thermally evaporated non-crystalline Cd50S50-xSex thin films, J. Alloys Compd. 648 (2015) 280–290.

[45] K.A.N. Duerloo, M.T. Ong, E.J. Reed, Intrinsic piezoelectricity in two-dimensional materials, J. Phys. Chem. Lett. 3 (2012) 2871–2876.

[46] C.R. Dhas, R. Venkatesh, R. Sivakumar, A. Moses, E. Raj, C. Sanjeeviraja, Effect of solution molarity on optical dispersion energy parameters and electrochromic performance of Co_3O_4 films, Opt. Mater. 72 (2017) 717–729.

[47] H.G. Tompkins, W.A. McGahan, Spectroscopic Ellipsometry and Reflectometry, John Wiley and Sons Inc., New York, 1999.

[48] B. Ouni, A. Boukhachem, S. Dabbous, A. Amlouk, K. Boubaker, M. Amlouk, Some transparent semi-conductor metal oxides: comparative investigations in terms of Wemple - DiDomenico parameters, mechanical performance and Amlouk - boubaker opto-thermal expansivity, Mater. Sci. Semicond. Process. 13 (2010) 281–287.

[49] H. Souissi, O. Taktak, M. Khalfa, A. Oueslati, S. Kammoun, M. Gargouri, Experimental and optical studies of the new organic inorganic bromide: $[(C_3H_7)_4N]_2CoBr_4$, Opt. Mater. 129 (2022) 112513.

[50] N. Mahfoudh, K. Karoui, A. BenRhaiem, Optical studies and dielectric response of $[DMA]_2MCl_4$ (M = Zn and Co) and $[DMA]_2ZnBr_4$, RSC Adv. 11 (2021) 24526–24535.

[51] R. Mguedla, A. Ben Jazia Kharrat, S. Kammoun, K. Khirouni, W. Boujelben, Optical studies of multiferroic HoCrO3 perovskite compound for optoelectronic device applications, Opt. Mater. 119 (2021) 111311.

[52] H. Souissi, S. Kammoun, Theoretical study of the electronic structure of a tetragonal chromium (III) complex, J. Lumin. 131 (2011) 2515–2520.

[53] O. Taktak, H. Souissi, S. Kammoun, Electronic structure and Fano antiresonance of chromium Cr (III) ions in alkali silicate glasses, J. Lumin. 161 (2015) 368–373.

[54] O. Taktak, H. Souissi, O. Maalej, B. Boulard, S. Kammoun, Fano's antiresonance and crystal-field study of Cr^{3+} in metaphosphate glasses, J. Lumin. 180 (2016) 183–189.

[55] H. Souissi, O. Taktak, S. Kammoun, Crystal field study of Chromium (III) ions doped antimony phosphate glass: fano's antiresonnance and Neuhauser models, Indian J. Phys. 92 (9) (2018) 1153–1160.

[56] O. Taktak, H. Souissi, S. Kammoun, Optical properties of the phosphors $Zn_2SnO_4:Cr^{3+}$ with near-infrared long-persistence phosphorescence for bio-imaging applications, J. Lumin. 228 (2020) 117563.

[57] O. Taktak, H. Souissi, S. Kammoun, Optical absorption properties of ZnF_2-RO-TeO_2 (R = Pb, Cd and Zn) glasses doped with chromium (III): neuhauser model and crystal field study, Opt. Mater. 113 (2021) 110682.

[58] Y. Li, Y. Li, R. Chen, K. Sharafudeen, S. Zhou, M. Gecevicius, H. Wang, G. Dong, Y. Wu, X. Qin, J. Qiu, Tailoring of the trap distribution and crystal field in Cr^{3+}-doped non-gallate phosphors with near-infrared long-persistence phosphorescence, NPG Asia Mater. 7 (2015) e180.

[59] H. Souissi, O. Taktak, S. Kammoun, Theoretical study by analytical equations of optical properties of the phosphors Zn_2SnO_4 codoped with Cr^{3+} and (Al^{3+} or Eu^{3+}) via the crystal field control, Opt. Mater. 121 (2021) 111529.

[60] M. Kumar, S.K. Gupta, An insight into optical spectroscopy of intense green emitting $ZnAl_2O_4:Tb^{3+}$ nanoparticles: photo, thermally stimulated luminescence and EPR study, J. Lumin. 168 (2015) 151–157.

[61] Y. Sun, J. Xu, R. Xi, H. Zhang, L. Liu, X. Xu, X. Fang, X. Wang, Unraveling the intrinsic reasons Promoting the reactivity of $ZnAl_2O_4$ spinel by Fe and Co for CO oxidation, Catal. Surv. Asia 25 (2021) 180–191.

[62] D. Zhang, Q. Guo, Y. Ren, C. Wang, Q. Shi, Q. Wang, X. Xiao, W. Wang, Q. Fan, Influence of inversion defects and Cr–Cr pairs on the photoluminescent performance of $ZnAl_2O_4$ crystals, J. Sol. Gel Sci. Technol. 85 (2018) 121–131.

[63] M. Popa, G. Schmerber, D. Toloman, M.S. Gabor, A. Mesaros, T. Petrişor, Magnetic and electrical properties of undoped and holmium doped ZnO thin films grown by sol-gel method, Adv. Eng. Forum 8–9 (2013) 301–308.